Numerical study of low pressure air plasma in an actuated channel

Tomas Houba and Subrata Roy[a)]
Applied Physics Research Group, Department of Mechanical and Aerospace Engineering, University of Florida, Gainesville, Florida 32611, USA

(Received 1 October 2015; accepted 3 December 2015; published online 18 December 2015)

A model for air plasma discharge based on drift-diffusion with local mean energy approximation is described. The model consists of 7 species and 18 reactions. The code is benchmarked with experimental and numerical results for low pressure glow discharge in a cylindrical tube. The code is used to simulate the discharge produced by a wire placed in a rectangular channel with grounded electrodes at the top and bottom walls. The discharge is concentrated near the wire. The actuator acts on the neutral gas through a body force and Joule heating. Around 80%–90% of the electrical power is converted to Joule heating of the neutral gas and the wall. The actuator produces a body force on the order of 0.1 mN/m. The effectiveness of the actuator increases from 100 to 300 V, and plateaus from 300 to 600 V. The results of the study suggest a further exploration of the channel concept. © *2015 AIP Publishing LLC*. [http://dx.doi.org/10.1063/1.4938023]

I. INTRODUCTION

The air flow produced by a gas discharge, known as the "electric wind," has been known since the early 1700s.[1] A device which uses a gas discharge to add momentum and energy to a fluid flow is known as a plasma actuator. The actuator creates a gas discharge by applying a sufficient voltage difference between two electrodes, ionizing the fluid in the vicinity. The bulk of research carried out on plasma actuators in more recent years has focused on their application to flow control.[2] Plasma actuators have been shown to delay transition in motorized glider flight tests,[3] and there is ongoing work to implement the actuators in real world applications.

A plasma pump can be created by placing plasma actuators inside a channel. The actuator can consist of plate electrodes,[4] wire electrodes,[5,6] or needle electrodes.[7] The advantages of producing a fluid flow in this manner include low power consumption, instantaneous response, and a lack of moving parts. The technology is also suitable for miniaturization. In this work, the plasma discharge in a channel produced by a wire electrode is studied numerically under lower than atmospheric pressure condition. The simulation of the plasma is performed using the fluid model with the drift-diffusion approximation. The most typical air plasma chemistry model used in fluid simulations contains three charged species, which are a positive ion, a negative ion, and an electron.[8,9] More complex models which include additional species have also been considered.[10,11] The model chosen to simulate the channel geometry in this work is first validated with experimental data.[12] The model is then applied to the new geometry, and the characteristics of the plasma discharge are studied. Finally, thrust inducement is predicted for the plasma actuated channel.

II. METHODOLOGY

A. Air chemistry model

The numerical model for the air plasma assumes a weakly ionized gas composed of positive ions, negative ions, and electrons. The air chemistry model in this work is based on the models by Mahadevan and Raja[11] and Pancheshnyi *et al.*[13] with several simplifying assumptions. The positive ions considered in the study include the two main ions N_2^+ and O_2^+, and the cluster ions N_4^+ and O_4^+. The $O_2^+N_2$ cluster ion is not considered in the model, because the simulations by Mahadevan and Raja[11] which include the ion show that its number density is not significant at the given conditions. When the ion was included in the current model, virtually no change in computed discharge current was observed. The negative species consist of the oxygen ions O^- and O_2^- along with electrons. The model presented by Mahadevan and Raja[11] also includes the solution of the neutral molecules N_2, O_2, and O. It is assumed that the number densities of N_2 and O_2 remain approximately constant due to the low degree of ionization. The concentration of the monoatomic oxygen O is also not computed, because the species does not appear as a reactant in the set of reactions considered. These simplifications help reduce the computational effort necessary to obtain results.

The reactions used in the present work are given in Table I. The reactions which involve electrons as reactants are calculated as a function of the mean electron energy. The free software BOLSIG+[14] is used to obtain the rates of a majority of the electron-driven reactions. A dry air mixture of 80% nitrogen and 20% oxygen is assumed. The excitation reactions include the effects of multiple excited N_2 and O_2 species, and the expressions for these reaction rates are provided by Mahadevan and Raja.[11] The remaining reaction rates are obtained from Ref. 15. A majority of the reaction rates involving only heavy species are a function of the gas temperature. The ions are assumed to be in thermal equilibrium with the neutrals, so the ion temperature is identical to the gas temperature.

B. Governing equations

The continuity equation that is solved for each plasma species is given as

[a)]Electronic mail: roy@ufl.edu. URL: http://aprg.mae.ufl.edu/roy/.

TABLE I. Air chemistry model.

	Formula	Reaction type	Reference
1	$N_2 + e^- \rightarrow N_2^+ + 2e^-$	Impact ionization	BOLSIG+[14]
2	$O_2 + e^- \rightarrow O_2^+ + 2e^-$	Impact ionization	BOLSIG+[14]
3	$N_2^+ + N_2 + M \rightarrow N_4^+ + M$	Ion-neutral association	Kossyi *et al.*[15]
4	$O_2^+ + O_2 + M \rightarrow O_4^+ + M$	Ion-neutral association	Kossyi *et al.*[15]
5	$O_2 + e^- \rightarrow O^- + O$	Electron attachment	BOLSIG+[14]
6	$2O_2 + e^- \rightarrow O_2^- + O_2$	Electron attachment	Kossyi *et al.*[15]
7	$N_2^+ + O_2 \rightarrow O_2^+ + N_2$	Charge exchange	Kossyi *et al.*[15]
8	$N_4^+ + O_2 \rightarrow O_2^+ + 2N_2$	Charge exchange	Kossyi *et al.*[15]
9	$O_2^+ + O^- \rightarrow O_2 + O$	Ion-ion recombination	Kossyi *et al.*[15]
10	$O_2^+ + O_2^- + M \rightarrow 2O_2 + M$	Ion-ion recombination	Kossyi *et al.*[15]
11	$O_4^+ + O_2^- + M \rightarrow 3O_2 + M$	Ion-ion recombination	Kossyi *et al.*[15]
12	$O_4^+ + O_2^- \rightarrow 3O_2$	Ion-ion recombination	Kossyi *et al.*[15]
13	$O_2^+ + e^- \rightarrow 2O$	Ion-electron recombination	Kossyi *et al.*[15]
14	$O_4^+ + e^- \rightarrow 2O_2$	Ion-electron recombination	Kossyi *et al.*[15]
15	$O_2 + e^- \rightarrow 2O$	Dissociation	BOLSIG+[14]
16	$O_2 + e^- \rightarrow O + O^*$	Dissociation	BOLSIG+[14]
17	$N_2 + e^- \rightarrow N_2^* + e^-$	Excitation	Mahadevan[11]
18	$O_2 + e^- \rightarrow O_2^* + e^-$	Excitation	Mahadevan[11]

$$\frac{\partial n_k}{\partial t} + \nabla \cdot \boldsymbol{\Gamma}_k = S_k. \tag{1}$$

The right-hand side of Eq. (1) contains the source and sink terms which represent the air chemistry. The mean electron energy used in the reaction rate coefficient calculations is obtained using the electron energy equation, which is written in the form recommended by Hagelaar and Pitchford[16]

$$\frac{\partial n_\varepsilon}{\partial t} + \nabla \cdot \boldsymbol{\Gamma}_\varepsilon = -\boldsymbol{\Gamma}_e \cdot \boldsymbol{E} + S_\varepsilon. \tag{2}$$

The first term on the right-hand side of Eq. (2) is the Joule heating, which is responsible for adding energy to the electrons. The second term contains electron energy losses due to the inelastic and elastic collisional processes. The collisional term has a standard form which is given by Rafatov *et al.*,[17] for example.

The flux terms in Eqs. (1) and (2) are approximated using the drift-diffusion model, which separates the flux into a drift part proportional to the electric field, and a diffusive part. The flux is written in the form

$$\boldsymbol{\Gamma}_k = Z_k n_k \mu_k \boldsymbol{E} - D_k \nabla n_k. \tag{3}$$

For the electron energy flux, $Z_\varepsilon = Z_e = -1$. The electron mobility and diffusion coefficients are calculated as a function of the mean electron energy using BOLSIG+.[14] The electron energy mobility and diffusion are directly related to the electron properties through the relations $\mu_\varepsilon = (5/3)\mu_e$ and $D_\varepsilon = (5/3)D_e$. All of the ion transport properties are computed as a function of the reduced electric field. The mobility for the N_2^+, O_2^+, and O^- ions are obtained from Ref. 18. The N_4^+ mobility is taken from Ref. 19, and the O_4^+ mobility is assumed to be identical. The ion diffusion coefficients are assumed to behave according to the Einstein relation.

The system of equations is closed by the solution of the electrostatic Poisson equation

$$-\nabla \cdot (\varepsilon \nabla \phi) = e \sum_k Z_k n_k. \tag{4}$$

The governing equations are written in a non-dimensional form using a reference number density of $10^{15}\,\mathrm{m}^{-3}$, electric potential of 1 V, length scale of 1 m, and timescale of 10^{-6} s.

The ionization source rates obtained from the solution of the governing equations are used to obtain the photoionization source terms. Photoionization has been studied previously at atmospheric pressure in literature,[20] and it was incorporated in the present model in an effort to bring in additional physics. The photoionization model used in this work was proposed by Bourdon *et al.*[21] and has been previously used in dielectric barrier discharge (DBD) plasma actuator simulations.[22] The photoionization source term is written using the third order approximation

$$S_{ph} = p_{O2} c \sum_{k=1}^{3} A_k \Psi_{0,k}, \tag{5}$$

where P_{O2} is the partial pressure of O_2 in air and c is the speed of light. The photon distribution function $\Psi_{0,k}$ is a combination of two functions $\phi_{1,k}$ and $\phi_{2,k}$

$$\Psi_{0,k} = \frac{\gamma_2 \phi_{1,k} - \gamma_1 \phi_{2,k}}{\gamma_2 - \gamma_1}. \tag{6}$$

The functions are calculated using a solution of Helmholtz equations of the form

$$\begin{aligned} \nabla^2 \phi_{1,k} - C_{11,k} \phi_{1,k} &= -C_{12,k} S_{iz} \\ \nabla^2 \phi_{2,k} - C_{21,k} \phi_{2,k} &= -C_{22,k} S_{iz}. \end{aligned} \tag{7}$$

The right-hand side of Eq. (7) contains the source term related to the rate of ionization. The parameters in Eqs. (5)–(7) and the boundary conditions for Eq. (7) are taken from Ref. 21. In total, three coupled pairs of Helmholtz equations are solved to obtain the photoionization source term defined by Eq. (5).

C. Boundary conditions

The boundary conditions for the plasma conservation laws are specified through the definition of the flux normal to the boundary. The wall normal vector is labeled $\boldsymbol{n}_w$. At the cathode boundary, the electron flux is calculated as

$$\boldsymbol{\Gamma}_e \cdot \boldsymbol{n}_w = \frac{1}{4} n_e v_{th,e} - \sum_s \gamma_s \boldsymbol{\Gamma}_s \cdot \boldsymbol{n}_w. \tag{8}$$

The first term on the right hand side of Eq. (8) is the thermal flux, and the second term is the secondary electron emission, which is calculated only for the N_2^+ and O_2^+ ion fluxes. For the anode boundary, the secondary emission term is zero. For the ions, the boundary flux at the anode and the cathode is

$$\boldsymbol{\Gamma}_k \cdot \boldsymbol{n}_w = \frac{1}{4} n_k v_{th,k} + \alpha Z_k n_k \mu_k \boldsymbol{E} \cdot \boldsymbol{n}_w, \tag{9}$$

where α is equal to one if the second term points toward the wall, and zero otherwise. Finally, the electron energy flux is

$$\boldsymbol{\Gamma}_\varepsilon \cdot \boldsymbol{n}_w = 2\frac{k_B T_e}{e}\boldsymbol{\Gamma}_e \cdot \boldsymbol{n}_w. \quad (10)$$

The normal component of the electric field, species flux, and electron energy flux is taken to be zero at the outer domain boundaries that are not solid. At a dielectric boundary, the species impacting the surface are assumed to recombine instantly with the dielectric material. The surface charge at the dielectric is then computed based on the relation

$$\frac{d\sigma}{dt} = -\sum_k Z_k \boldsymbol{\Gamma}_k \cdot \boldsymbol{n}_w. \quad (11)$$

The surface charge contributes to the right-hand side source term of the Poisson equation for cells neighboring the dielectric surface.

D. Numerical methodology

The system of governing equations is solved using the finite volume module of the Multiscale Ionized Gas (MIG) code. The face fluxes are approximated using the first order accurate Scharfetter-Gummel scheme.[23] The steady Poisson equation is coupled to the unsteady charged species conservation laws. This coupling poses a computational challenge in time marching the solution due to the frequent necessity to update the electric potential. The electric potential is updated based on Maxwell time, given by

$$\tau_M = \frac{\varepsilon_0}{e\sum_k n_k \mu_k}. \quad (12)$$

The ion and electron equations are integrated in time using a second order explicit Runge-Kutta method in between successive updates of the electric potential. The value of the step size changes based on the stability condition of the simulation. The time step restrictions imposed by the electrons and the air chemistry are much more strict than those required by the heavy species transport. The time integration of the heavy species fluxes is therefore carried out separately based on the most restrictive Courant-Friedrichs-Lewy (CFL) condition among the ions. The electrons and the chemical source terms are integrated based on the CFL condition imposed by the electron energy transport. The simulation is performed from uniform initial conditions for the species number densities and marched in time until the steady state is reached.

E. Geometry and grid

The governing equations are solved for the geometry shown in Fig. 1. A copper wire is placed at the centerline of a channel with a height of 5 cm. The grounded electrodes are placed at the top and the bottom of the channel. These electrodes have a length of 5 cm each, and the distance in the x-direction between the center of the wire and the leading edge of the grounded electrode is 10 cm. The simulation domain extends an additional 2 cm behind the wire in the x-direction. It is only necessary to solve one half of the domain numerically due to symmetry.

The computational grid consists of 221 × 181 rectangular cells with variable sizes. The smallest cell size in either direction is 10 μm, located in the proximity of the wire to resolve the large electric field in this region. The model approximates the wire cross-section as a square with sides of 80 μm, similar to a 40 AWG wire. All cells with centers located inside the wire are modeled as solid cells.

III. RESULTS AND DISCUSSION

A. Code benchmarking

The code was benchmarked for the test problem of DC glow discharge in a cylindrical tube. Lisovskiy and Yakovin[12] carried out experiments in which they studied the glow discharge inside a large diameter tube for a range of pressures and several discharge tube lengths. The cylindrical tube chosen for the benchmark case had a length of 32 mm. The computational grid for the test case was varied from 100 to 400 computational cells stretched with the hyperbolic tangent function. The pressure was set to 0.6 Torr, and the neutral gas temperature was kept at 300 K. The geometry consists of a cathode at x = 0 and an anode at x = 32 mm. The particular length and pressure were chosen because the axial structure of the discharge is described for this case.[12] This experimental geometry was also simulated numerically in 2-D by Mahadevan and Raja.[11]

Due to the large diameter of the tube (100 mm) relative to the length, the discharge along the centerline of the tube was simulated in 1-D along the axial direction. To obtain the net current, the 1-D current density is multiplied by the cylindrical area normal to the discharge axis. Since the channel case is not in cylindrical coordinates, the choice of 1-D geometry avoids the necessity of discretizing the governing equations in the cylindrical coordinates for the radial direction. The 2-D spatial discretization is a direct extension of the 1-D case.

Fig. 2 shows a plot of the voltage drop between the electrodes versus the discharge current. The computed current shows a linear variation with voltage. The voltage-current line shows a slope that is similar to the other numerical result, with the difference that the current is higher for a

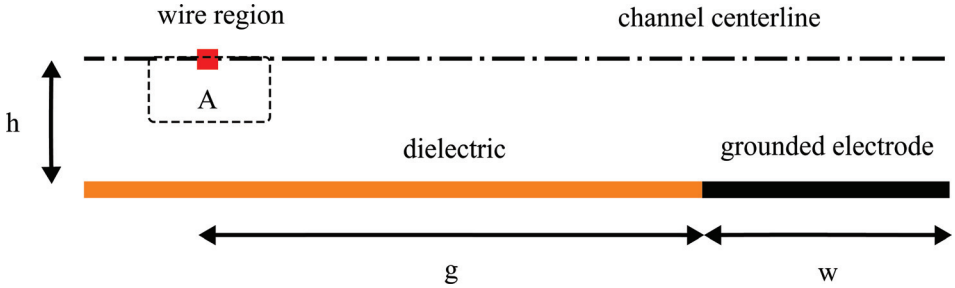

FIG. 1. The schematic of the actuator inside the channel.

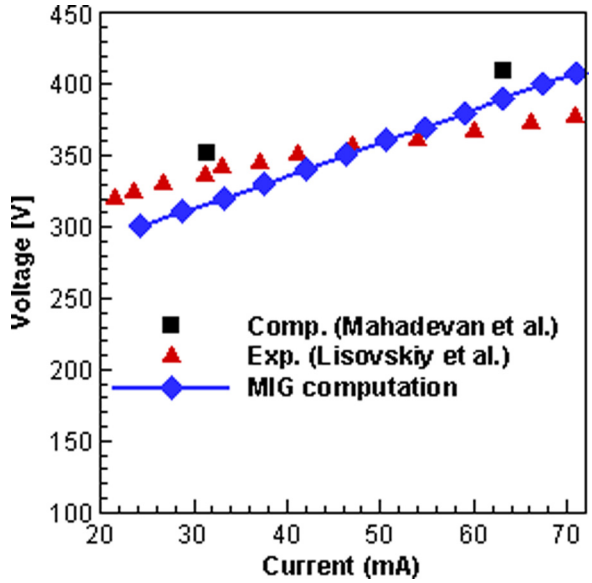

FIG. 2. Comparison of the current versus voltage for the DC glow discharge in a tube.

given voltage drop. This is to be expected, because the 1-D simulation will not lose any particles to the side walls. The slight differences between the slopes can be attributed to small differences between the models.

Fig. 3 shows a comparison of the positive ion number density distribution in the axial direction. The numerical profile of the positive ion density exhibits a double layer near the cathode region which is not observed in the experimental data, but has been computed by the simulation of Mahadevan and Raja.[11] The experimental number density profiles for the lower voltages experience a sharper drop-off than predicted by the numerical result, which can be partially attributed to the larger error of the drift-diffusion model in the sheath region. Despite these discrepancies, the number densities predicted by the numerical model fall in a similar range to the experimentally measured values.

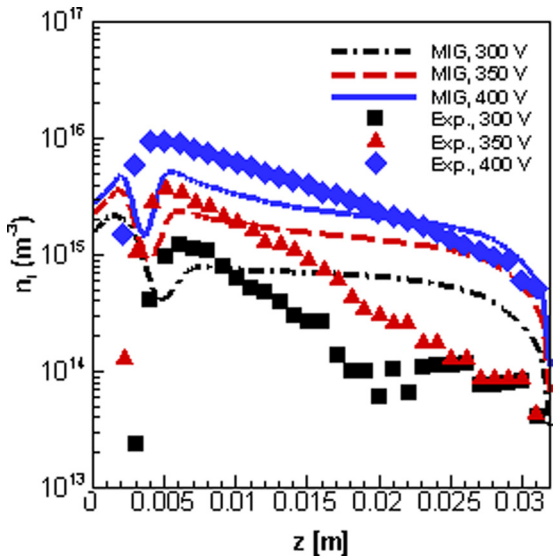

FIG. 3. Positive ion number density along the axial direction of the tube.**

Fig. 4 compares the electron temperature distribution in the axial direction. The experimental data for the three test voltages show a larger variation than the numerical results. The numerical data predict an electron temperature of about 1 eV in the bulk plasma region away from the electrodes. The electron temperature toward the electrodes rises at a slope comparable to the experimental measurements at 350 V. The profile of the electron temperature shows good qualitative agreement with the experiment.

The 1-D results were also compared with the results of Mahadevan and Raja[11] along the centerline of tube. Fig. 5 shows the charge and number density graph for a voltage of 408 V. The computed net charge shows a very good agreement with the published result. The primary difference occurs in the negatively charged species. In the MIG results, a larger number of electrons are predicted to attach to neutral atoms and form negative ions. This is reflected in a decreased electron number density and an increased negative

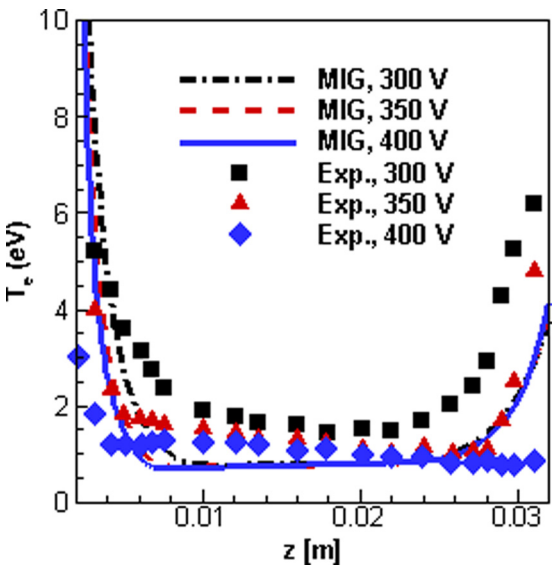

FIG. 4. Electron temperature along the axial direction of the tube.

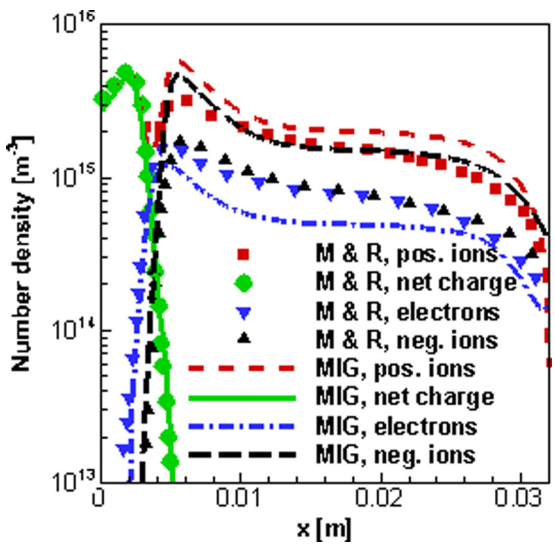

FIG. 5. Comparison of number density and charge at 408 V.

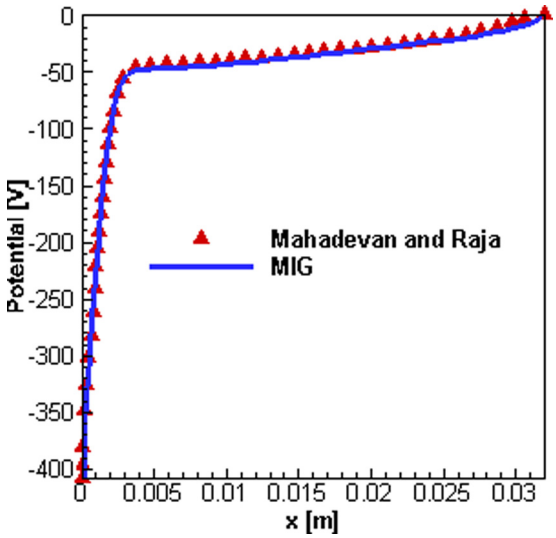

FIG. 6. Comparison of the electric potential at 408 V.

ion number density. Fig. 6 shows the electric potential for the two cases. Here, the comparison shows excellent agreement, which is to be expected based on the good match obtained for the net charge density.

The benchmark case produces reasonable values for the computed current, positive ion number density, and electron temperature compared with the experiment. In order to maintain a practical fidelity of the model, it should be applied at conditions similar to the experiment. Substantial deviations from the conditions of the experiment could cause larger errors and hinder the predictive capability of the model.

B. Plasma discharge in the channel

The model was applied to the wire and channel geometry described in Section II E. The wire is powered by a continuous DC voltage signal. The applied voltage was varied from 100 to 600 V. The pressure and temperature were set to 0.6 Torr and 300 K, respectively, to match the operating conditions for which the model was benchmarked.

Figs. 7–9 display the number density contours for the electrons, positive ions, and negative ions for the wire region denoted in Fig. 1. The contours are shown for the smallest and largest applied voltages. The contours of the species densities show that the discharge is concentrated in the vicinity of the wire, which is the region of the highest electric field. The electron density at 600 V peaks at around 6×10^{16} m^{-3}, while the 100 V case reaches peak values of about 9×10^{15} m^{-3}. The positive ions in Fig. 8 show a similar spatial density profile, with the exception of the immediate neighborhood of the anode wire. In this region, the positive ion number density shows a large drop-off. The negative ion number density is plotted in Fig. 9. The results indicate that the number densities of the negative ions are on average about an order of magnitude below those of the electrons and positive ions. A detailed breakdown of the positive and negative ion species for 600 V is provided in Figs. 10 and 11.

Fig. 12 shows the comparison of the electron temperature for the two cases. As expected, the region near the wire contains hotter electrons. At 100 V, the electron temperature in the majority of the domain does not exceed 1 eV. At 600 V, the region of high electron temperature extends farther from the wire, and the electron temperature near the wire is above 2 eV.

The photoionization source term over the simulation domain is presented in Fig. 13. The photoionization occurs primarily in the cathode region of the discharge. The photoionization rate at 600 V is over two orders of magnitude higher than the rate computed at 100 V, which shows an increasing role of photoionization with increasing voltage. Despite the large increase, the photoionization does not appear to have a significant impact for the given conditions and voltage range. Even at the highest voltages considered, the photoionization rate is still just a small fraction of the ionization rate.

C. Discharge characteristics

The plasma discharge in the channel was analyzed to identify the performance characteristics. The discharge current is obtained by integrating the species current flowing through the electrode

$$I = 2e \int_L \left(\sum_k Z_k \boldsymbol{\Gamma}_k \cdot \boldsymbol{n}_w \right) dx. \tag{13}$$

The power is calculated from the relation $P = IV$, where V is the applied voltage. The net force per unit length is

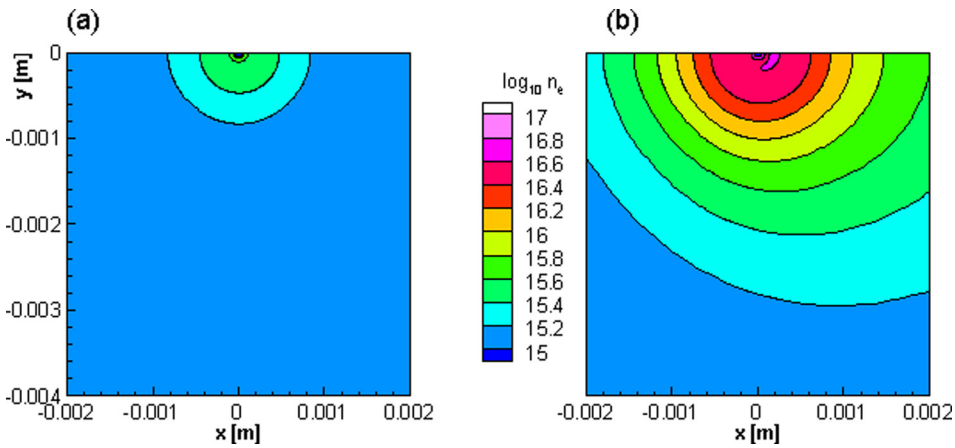

FIG. 7. Contour of the common logarithm of electron number density [log of m^{-3}] distribution in the wire region A at (a) 100 V and (b) 600 V.

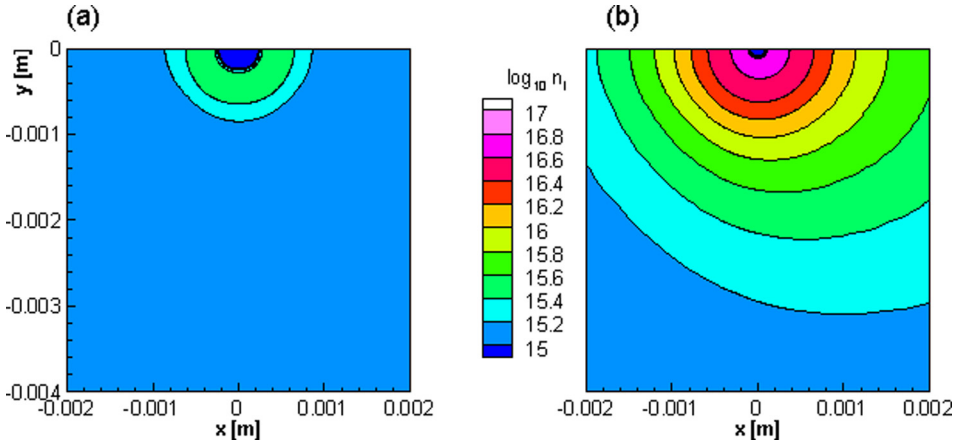

FIG. 8. Contour of the common logarithm of positive ion number density [log of m^{-3}] distribution in the wire region A at (a) 100 V and (b) 600 V.

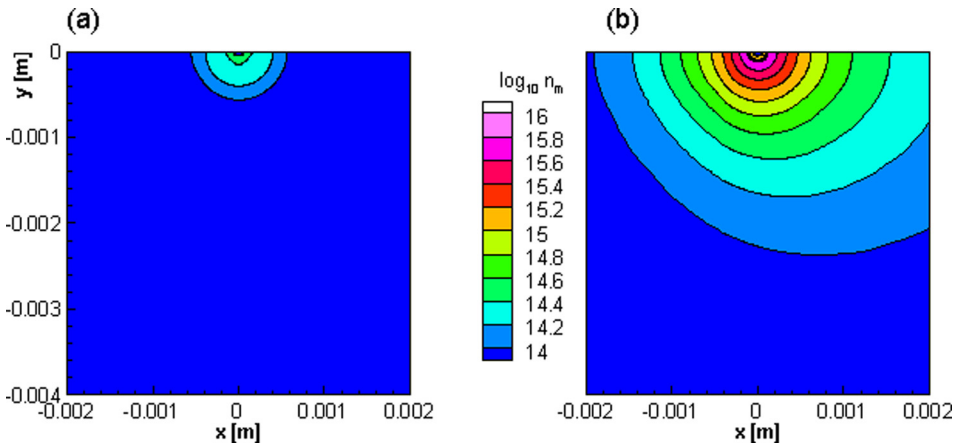

FIG. 9. Contour of the common logarithm of negative ion number density [log of m^{-3}] distribution in the wire region A at (a) 100 V and (b) 600 V.

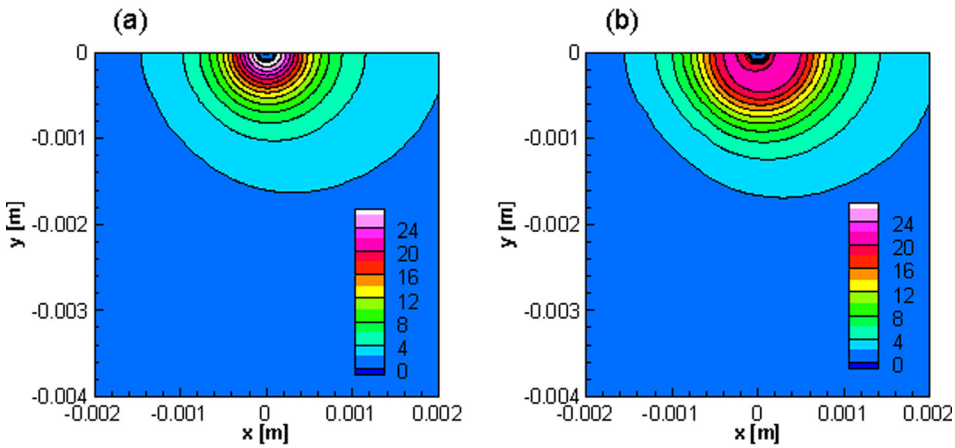

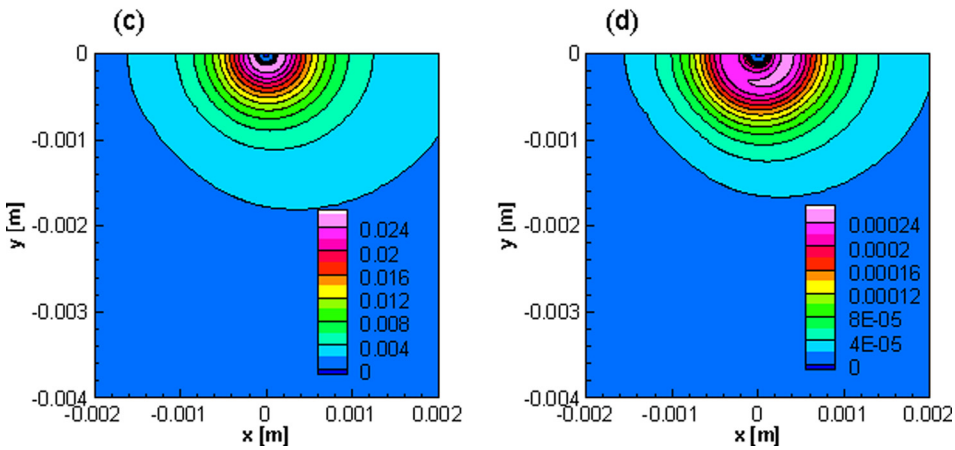

FIG. 10. Contours of the positive ion species number densities at 600 V. (a) N_2^+ [10^{15} m^{-3}], (b) O_2^+ [10^{15} m^{-3}], (c) N_4^+ [10^{15} m^{-3}], and O_4^+ [10^{15} m^{-3}].

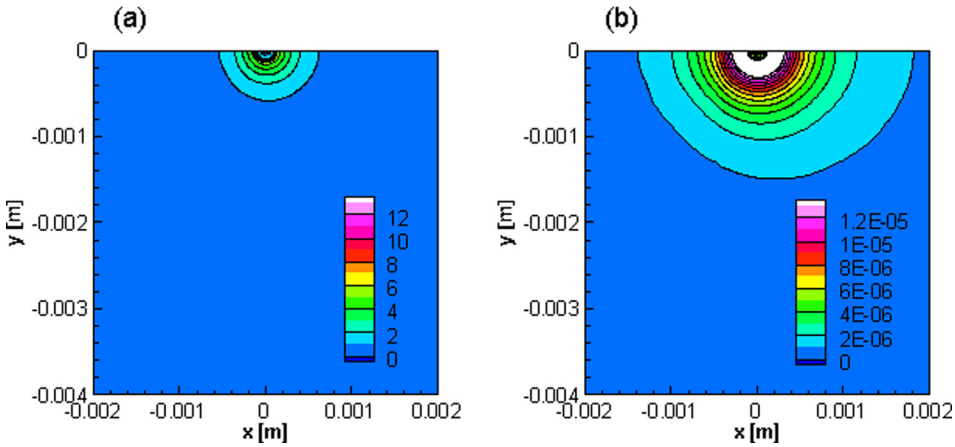

FIG. 11. Contours of the negative ion species number densities at 600 V. (a) O^- [10^{15} m^{-3}] and O_2^- [10^{15} m^{-3}].

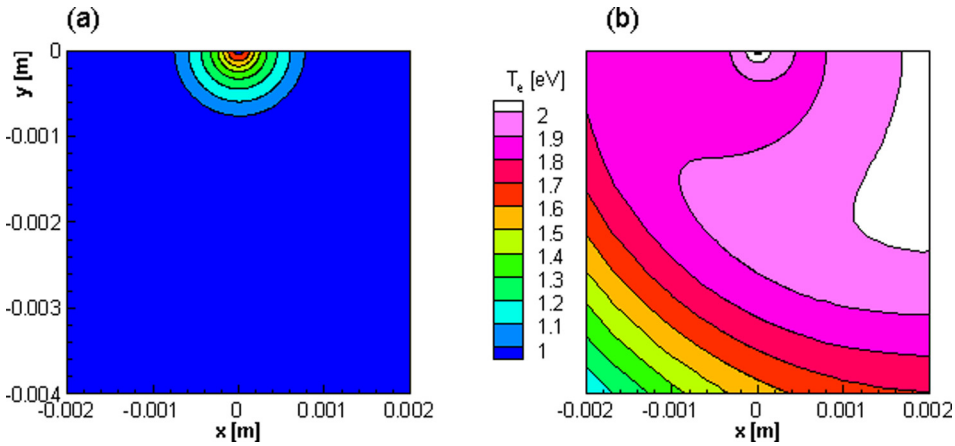

FIG. 12. Contour of the electron temperature [eV] distribution in the wire region A at (a) 100 V and (b) 600 V.

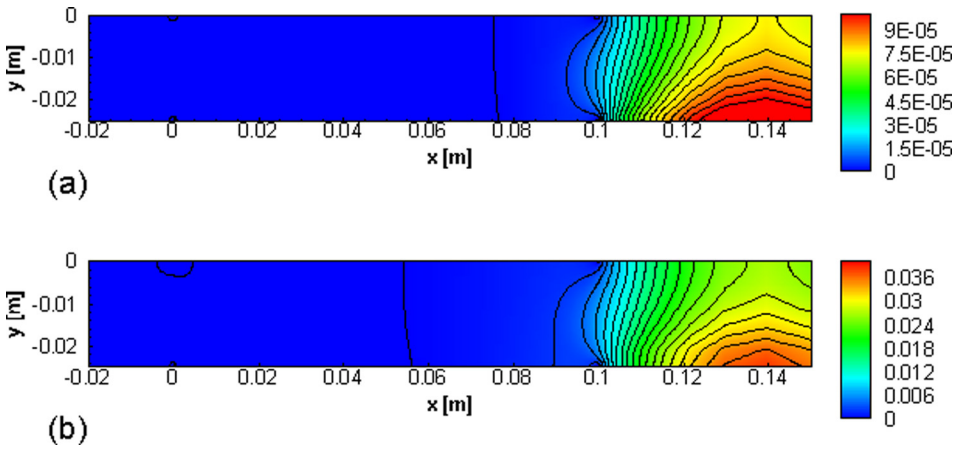

FIG. 13. Contour of the non-dimensional photoionization source term distribution in the computational domain at (a) 100 V and (b) 600 V.

obtained by integrating the net charge times the electric field over the domain. The effectiveness is defined as $\zeta = F_x/P$

$$F_x = 2e \int\int_A \left(\sum_k Z_k n_k \right) E_x dA. \quad (14)$$

The total heating due to the plasma is calculated from the ion Joule heating term integrated over the domain. The heating term is written as

$$Q = 2e \int\int_A \sum_{k \neq e} (\boldsymbol{\Gamma}_k \cdot \boldsymbol{E}) dA. \quad (15)$$

The electrical parameters for the channel actuator are presented in Fig. 14. The discharge current is computed by integrating the cathode current. Fitting a linear curve to the data yields an R-squared value of 0.997, implying that the deviation from the linear current-voltage behavior is not too large. The power consumed by the channel varies from roughly 4 W to 70 W per meter of the electrode over the voltage range studied.

The trend of the effect of the discharge on the neutral gas is plotted versus the applied voltage in Fig. 15. The body force and heating appear to follow a power relationship with voltage, with exponent values around 1.6. The results indicate that over 80% of the power deposited into the discharge goes into the ion Joule heating. A fraction of this energy is used to heat the gas, while

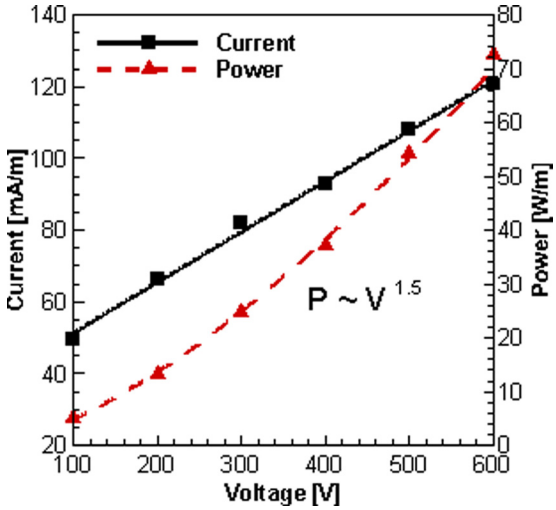

FIG. 14. Discharge current and consumed power as a function of the applied voltage.

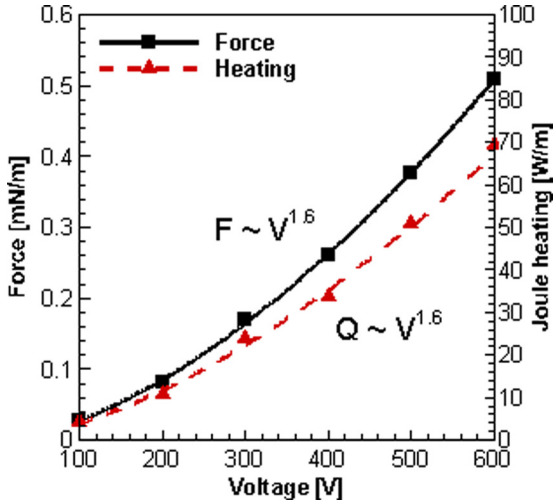

FIG. 15. Body force and Joule heating of the gas as a function of the applied voltage.

the rest will be absorbed by the dielectric material. For example, in the xenon discharge at 100 Torr, it was estimated that 25% of the energy was deposited in the neutral gas.[24] In this work, a conservative approach is taken to obtain the upper bound for the gas heating, and the entire ion Joule heating is considered. The remainder of the discharge power goes into the electrons, which lose energy in inelastic collisions due to the various ionization, attachment, and excitation reactions. If the velocity of the neutral gas induced by the plasma does not exceed values on the order of 1 m/s, the kinetic energy gains will not account for more than 1% of the total power.

The body forces produced by the channel are on the order of 0.1 mN per meter. This body force is smaller than what plasma actuators have been observed to produce at atmospheric pressure, but a decrease in the generated thrust of plasma actuators at low pressures has been observed.[25] It should be noted that the body force is computed based on the number density, which can show up to an order of magnitude difference from the experimental data in the benchmark

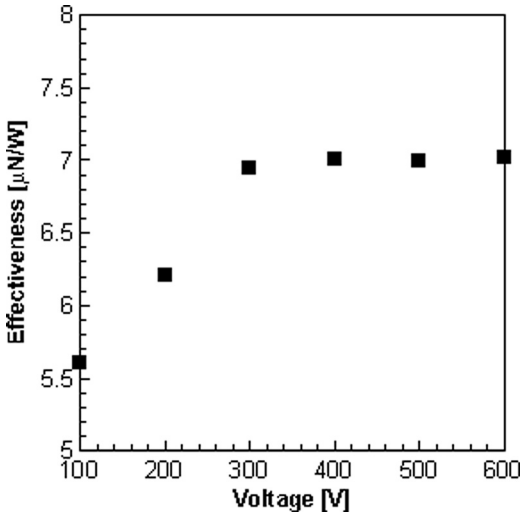

FIG. 16. Effectiveness of the actuated channel as a function of the applied voltage.

case. Therefore, the body force calculation only provides an estimate for the actuator thrust.

Fig. 16 shows the effectiveness of the actuator. The effectiveness of the plasma channel increases until 300 V. Beyond this point, the thrust to power ratio of the actuator appears to saturate. This can be attributed to the increased percentage of the electrical power being converted into Joule heating. At 100 V, the percentage converted to heating is about 81%, while at 600 V this percentage increases to 95%. The large fraction of the discharge power deposited into the neutral gas suggests that the assumption of the constant gas temperature in the model has to be carefully considered. It may be advisable to solve an additional equation for the neutral gas temperature on the heavy species timescale.

IV. CONCLUSIONS

The plasma actuator configuration presented in this work was shown to inject momentum and energy to the neutral gas in the channel. The wire region dictates the dynamics of the discharge. For the entire voltage range, the charged species are concentrated near the wire and the region also has the highest electron temperature. The majority of the energy in this particular regime was observed to go to the gas heating. The effectiveness of the actuator increased until 300 V, at which point no further increases were observed.

The channel-wire configuration shows promise as a potential fluid pump. The numerical study can be extended to higher pressures to determine if the effectiveness of the setup can be increased. A high pressure study requires a modified air chemistry model to account for reaction channels which are not present at lower pressures. The expanded air chemistry model can also be used to estimate other quantities of practical interest, such as the generation of ozone and NO_x gases. Future simulations will also focus on running three-dimensional simulations of more complex channel configurations.

[1]M. Robinson, Am. J. Phys. **30**, 366 (1962).
[2]T. C. Corke, C. L. Enloe, and S. P. Wilkinson, Annu. Rev. Fluid Mech. **42**, 505 (2010).

[3]A. Duchmann, B. Simon, C. Tropea, and S. Grundmann, AIAA J. **52**, 358 (2014).
[4]M. Riherd and S. Roy, J. Appl. Phys. **112**, 053303 (2012).
[5]A. Yabe, Y. Mori, and K. Hijikata, AIAA J. **16**, 340 (1978).
[6]N. Campbell and S. Roy, Appl. Phys. Lett. **105**, 132906 (2014).
[7]P. Zhao, S. Portugal, and S. Roy, Appl. Phys. Lett. **107**, 033501 (2015).
[8]A. V. Likhanskii, M. N. Shneider, S. O. Macheret, and R. B. Miles, J. Appl. Phys. **103**, 053305 (2008).
[9]T. Unfer and J. P. Boeuf, J. Phys. D: Appl. Phys. **42**, 194017 (2009).
[10]K. P. Singh and S. Roy, J. Appl. Phys. **101**, 123308 (2007).
[11]S. Mahadevan and L. L. Raja, J. Appl. Phys. **107**, 093304 (2010).
[12]V. A. Lisovskiy and S. D. Yakovin, Plasma Phys. Rep. **26**, 1066 (2000).
[13]S. Pancheshnyi, M. Nudnova, and A. Starikovskii, Phys. Rev. E **71**, 016407 (2005).
[14]See www.bolsig.laplace.univ-tlse.fr for BOLSIG+.
[15]I. A. Kossyi, A. Y. Kostinsky, A. A. Matveyev, and V. P. Silakov, Plasma Sources Sci. Technol. **1**, 207 (1992).
[16]G. J. M. Hagelaar and L. C. Pitchford, Plasma Sources Sci. Technol. **14**, 722 (2005).
[17]I. Rafatov, E. A. Bogdanov, and A. A. Kudryavtsev, Phys. Plasmas **19**, 093503 (2012).
[18]D. Nelson, M. Benhenni, O. Eichwald, and M. Yousfi, J. Appl. Phys. **94**, 96 (2003).
[19]A. Bekstein, M. Benhenni, M. Yousfi, O. Ducasse, and O. Eichwald, Eur. Phys. J.: Appl. Phys. **42**, 33 (2008).
[20]A. A. Kulikovsky, J. Phys. D: Appl. Phys. **33**, 1514 (2000).
[21]A. Bourdon, V. P. Pasko, N. Y. Liu, S. Celestin, P. Segur, and E. Marode, Plasma Sources Sci. Technol. **16**, 656 (2007).
[22]A. V. Likhanskii, Ph.D. thesis, Pennsylvania State University, 2009.
[23]D. L. Scharfetter and H. K. Gummel, IEEE Trans. Electron Devices **16**, 64 (1969).
[24]J. P. Boeuf, L. C. Pitchford, and K. H. Schoenbach, Appl. Phys. Lett. **86**, 071501 (2005).
[25]J. Soni and S. Roy, Appl. Phys. Lett. **102**, 112908 (2013).